First Measurements of Hydrodynamic Instability Growth in Indirectly Driven Implosions at Ignition-Relevant Conditions on the National Ignition Facility

V. A. Smalyuk,[1] D. T. Casey,[1] D. S. Clark,[1] M. J. Edwards,[1] S. W. Haan,[1] A. Hamza,[1] D. E. Hoover,[2] W. W. Hsing,[1] O. Hurricane,[1] J. D. Kilkenny,[2] J. Kroll,[1] O. L. Landen,[1] A. Moore,[3] A. Nikroo,[2] L. Peterson,[1] K. Raman,[1] B. A. Remington,[1] H. F. Robey,[1] S. V. Weber,[1] and K. Widmann[1]

[1]*Lawrence Livermore National Laboratory, Livermore, California 94550, USA*

[2]*General Atomics, San Diego, California 92121, USA*

[3]*AWE Aldermaston, Reading, Berkshire RG7 4PR, United Kingdom*

(Received 4 December 2013; published 8 May 2014)

Ignition experiments have shown an anomalous susceptibility to hydrodynamic instability growth. To help understand these results, the first hydrodynamic instability growth measurements in indirectly driven implosions on the National Ignition Facility were performed at ignition conditions with peak radiation temperatures up to ~300 eV. Plastic capsules with two-dimensional preimposed, sinusoidal outer surface modulations of initial wavelengths of 240 (corresponding to a Legendre mode number of 30), 120 (mode 60), and 80 μm (mode 90) were imploded by using actual low-adiabat ignition laser pulses. The measured growth was in excellent agreement, validating 2D HYDRA simulations for the most dangerous modes in the acceleration phase. These results reinforce confidence in the predictive capability of calculations that are paramount to illuminating the path toward ignition.

DOI: 10.1103/PhysRevLett.112.185003 PACS numbers: 52.57.Fg

The current indirect-drive ignition point design on the National Ignition Facility (NIF) [1] uses a 1.6 MJ laser pulse at peak power of 410 TW to accelerate the deuterium-tritium (DT) fuel to a peak implosion velocity of ~370 km/s [2]. The implosion must achieve a temperature of $T_i > 5$ keV in the central hot spot and a high DT fuel compression with $\rho R_{\text{hot spot}} \sim 0.3$ g/cm^2 and $\rho R_{\text{fuel}} \sim 1.5$ g/cm^2 to achieve the predicted ignition neutron yield of ~20 MJ [2]. In recent high-compression experiments on the NIF, a fuel areal density of ~1.3 g/cm^2 has been achieved with a fuel velocity of ~330 km/s [3,4]. While these two key performance parameters were close to the ignition goal, the neutron yield was significantly lower than predicted [3,4]. The presence of ablator material mixed into the hot spot was correlated with reduced experimental yields and temperatures in the high-compression layered DT implosions [5–7]. These results demonstrated a critical role of hydrodynamic instabilities [8,9] in the performance degradation of ignition capsules. Multidimensional (2D and 3D) simulations of the cryogenic layered DT implosions, including measured capsule surface roughness and drive asymmetries, overpredicted measured yields by factors of ~5 to ~30 for high-compression implosions [10]. However, 2D simulations with large, unphysical multipliers (up to 3–5×) on the capsule surface roughness could degrade simulated yields down to the measured levels [10] but for reasons that are not yet understood.

There are several possible explanations for the need of a large multiplier on the initial surface perturbation for simulations to match experiments. The effective roughness could in fact be larger than assumed based on current metrology methods. The Rayleigh-Taylor [11–13] growth rates during the acceleration phase [8,9] or the preacceleration amplitudes established during the Richtmyer-Meshkov [14,15] instability phase could also be larger than simulated. Also, some possible seeds for instability growth, such as radiation asymmetry [16], dust grains, and other localized defects, and the effect of the membrane ("tent") used to support the capsule [17,18] were not included or may have been underestimated in the simulations. This Letter describes the first experiments to directly measure ablation-front hydrodynamic growth by using x-ray radiography of preimposed, 2D sinusoidal perturbations at the NIF. The measurements were focused on the fastest and most dangerous growing modulations corresponding to Legendre modes from 30 to 90. The results validated hydrodynamic growth in simulations during both the Richtmyer-Meshkov phase and the Rayleigh-Taylor phase at the outer ablation surface with capsule convergence of 2–3 at ignition conditions. This validation is critical to develop new robust designs capable of achieving thermonuclear ignition at the NIF.

Figure 1(a) shows the experimental configuration, which includes a hohlraum with a plastic capsule and a gold cone. The modulation growth was measured with through-foil x-ray radiography [19,20] using ~5.4-keV x rays generated by the vanadium backlighter located 12 mm from the target center. The experiments were conducted with the drives and conditions similar to those used in high-compression layered DT implosions [3]. They were designed to test the hydrodynamic growth predictions used to model these DT layered implosions that achieved fuel areal densities of

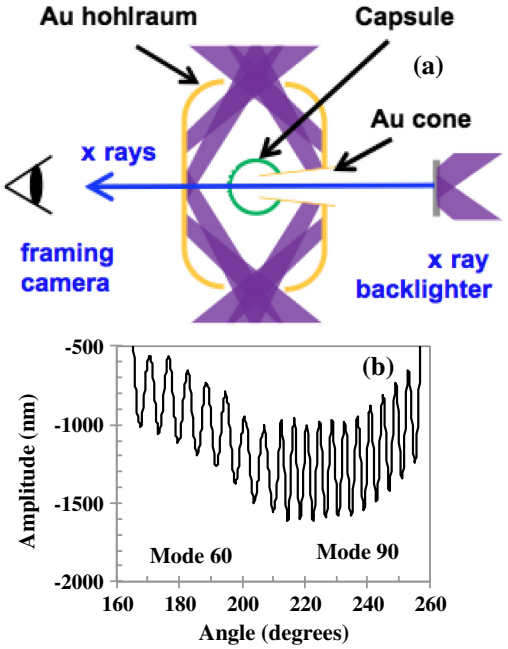

FIG. 1 (color online). (a) Experimental configuration. (b) The initial amplitude vs the azimuthal angle for side-by-side, 2D sinusoidal modulations with mode numbers of 60 and 90 (with initial wavelengths of 120 and 80 μm, respectively) for one of the capsules with ripple amplitudes of 0.25 and 0.3 μm, respectively.

$\sim$1.3 g/cm^2 at peak radiation temperatures of $\sim$300 eV [3]. The capsules had preimposed, 2D sinusoidal modulations at three wavelengths: 240 (corresponding to Legendre mode 30), 120 (mode 60), and 80 μm (mode 90). The gold cone constrained the backlighter x rays to pass through a single wall of the shell, enabling high-quality radiographs of the growing modulations. The thickness of the gold cone was 150 μm, while the 800-μm inner diameter at the tip of the cone set the field of view for the radiography. The initial modulation amplitudes of 0.75 and 1.7 μm were used in two shots with initial wavelengths of 240 and 120 μm, respectively. In another shot, side-by-side modulations at wavelengths of 120 and 80 μm had initial amplitudes of 0.25 and 0.3 μm, respectively.

Figure 1(b) shows the lineout of the initial capsule perturbation amplitude versus azimuthal angle used in the shot with side-by-side mode 60 and 90 sinusoidal modulations. The preimposed modulations were high-quality sinusoidal modulations with all higher harmonics kept below $\sim$5% of the amplitude of the fundamental sinusoidal modulations. The variations of the modulation amplitudes were below $\sim$10% over the whole area of interest for radiography. The nominal 209-μm thick plastic capsules with nominal 1120-μm outer radii had the same Si-doped layers, as used in the previous DT layered implosion [3]. An extra 14-μm thick CH layer was used to replace the 69-μm thick DT layer to maintain the same shell mass as in the layered DT implosions. Current experiments followed a campaign that characterized the implosion shock timing and symmetry, as described in Refs. [21–25]. Capsule and hohlraum details were also previously published (see Fig. 1 of Ref. [26]). The experiments were driven with the shaped, 21-ns long laser pulse with a peak power of $\sim$350 TW and a total laser energy of 1.3 MJ by using 184 beams of the NIF laser system. An additional eight overlapped beams were used to drive a 12.5-μm thick vanadium backlighter foil (located 12 mm from the capsule center) at a peak laser intensity of $\sim 5 \times 10^{14}$ W/cm^2 with a pulse and an experimental configuration similar to previous backlighting experiments on the NIF [21]. X rays of the vanadium K shell at $\sim$5.4 keV were used to radiograph growing capsule modulations. The differences included the additional gold cone, the backlighter material (vanadium vs germanium), and the reduced thickness (80- vs 160-μm) of the high-density carbon (HDC) window placed at the hohlraum wall directly opposite the cone. The 250-μm wide and 900-μm long HDC windows provided a clear line of sight for the backlighter x rays used for radiography.

Figure 2 shows examples of measured capsule x-ray radiographs captured on a framing camera for three different experiments with modes 30, 60, and side-by-side modes

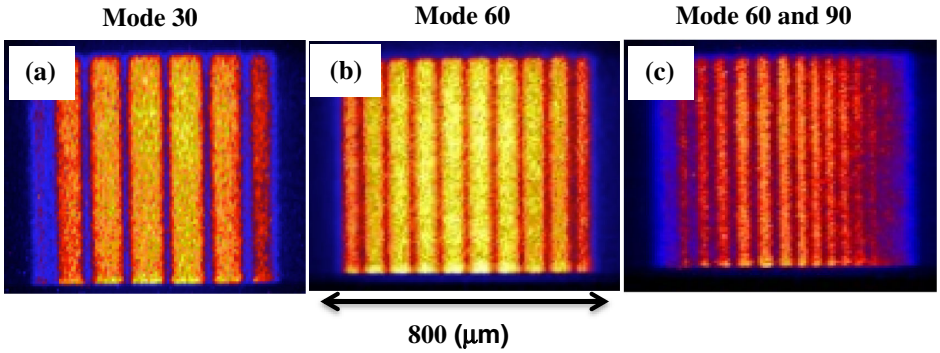

FIG. 2 (color online). Examples of measured radiographs are shown for three experiments with modulations at mode numbers of 30, 60, and side-by-side modes 60 and 90. The radiographs were taken at times of 20.3, 19.3, and 20.3 ns, respectively.

60 and 90 using 20-μm wide, 1000-μm long slits. Four slit images were captured in each shot at four different times. The slit was oriented vertically along the hohlraum axis, as were the capsule 2D modulations. The 250-μm vertical size of the HDC window defined the integration extent of the slit images, while the field of view in the horizontal direction was defined by the 800-μm inner diameter of the Au cone. The slit was positioned 100 mm from the target center, while the detector, a framing camera [27], was located 1300 mm from the target center, giving a magnification of ~12 for the imaging system. X-ray filters were used in these experiments both to protect the diagnostics from the debris generated by the hohlraum (using 150 μm polyimide filter) and to suppress x-ray emission above the vanadium K edge to improve image contrast (using 12.5-μm thick vanadium filters). The temporal resolution of the images system was 100 ps, limited by the framing camera resolution [27], while the spatial resolution was 20 μm in the horizontal direction, perpendicular to the slit. The x-ray background was measured by using an additional shot and was subtracted from the radiography images during data analysis. This background consisted of hard x rays generated by hot electrons (with energies >20 keV) produced by laser-plasma interaction processes in the hohlraum [28,29] and soft x rays (~5–10 keV) produced mainly between the capsule and the HDC window inside the hohlraum. The measured peak hard and soft x-ray backgrounds were ~10% and 2%, respectively, of the backlighter signal. The spectral purity of x rays used in the imaging system was measured with the absorption of the 30-μm thick aluminum strip placed in front of the framing camera on each shot. The measured strip attenuation was consistent with ~5.4-keV x rays generated by the K shell of the vanadium backlighter. To compare simulations with experimental results, the simulations were postprocessed to simulate the observed contrast of the 5.4-keV x rays, as discussed below. Optical-depth (OD) variations (used in the analysis below) were obtained by taking a natural logarithm of the framing-camera images after x-ray backgrounds were subtracted.

Figure 3 shows measured (symbols) and simulated (solid curves) modulation wavelengths as a function of time for experiments with mode 30, 60, and 90 modulations. The measurements were conducted for convergence ratios up to ~2, when the shell radius was decreased down to ~500 μm during the implosion. To determine the wavelengths, three central waves were used for each mode. Spherical effects of the shell imaging introduced a small error in determining the wavelengths, which was greater for lower modes due to a larger capsule area used in the analysis. Simulations of these experiments were performed with two plastic equation of state (EOS) models [30], LEOS 5400 and LEOS 5370. These 2D HYDRA simulations (symmetric about the hohlraum axis) are of the spherical capsule only, using a frequency-dependent x-ray source that was extracted from

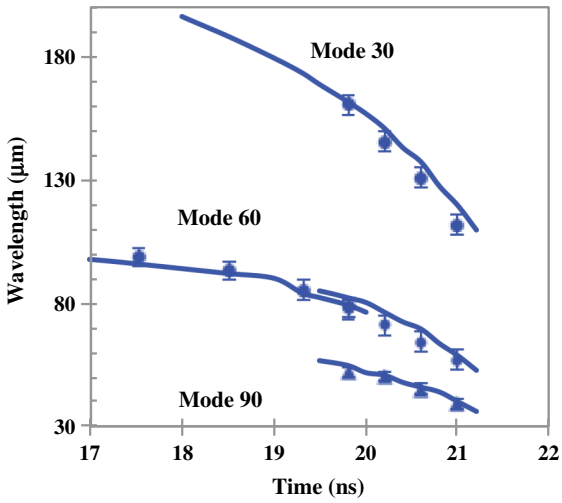

FIG. 3 (color online). Measured (plotting symbols) and simulated (smooth solid curves) modulation wavelengths as a function of time for experiments with mode 30, 60, and 90 modulations.

hohlraum simulations. The drive was then adjusted in two ways: the flux vs time was adjusted to fit the prior shock timing [24] and backlit implosion experiments [21], with different adjustments needed for each of the respective equations of state, and the brightness of the 2–3 keV M-band spectral feature was adjusted to agree with the measured brightness in this band. The simulations were performed by using measured surface modulations, with a total azimuthal range of 180° and angular resolution of up to 16 zones/degree. Solid curves in Fig. 3 represent simulations with LEOS 5400, which for this figure were essentially identical to the predictions with LEOS 5370. The convergence ratio (defined as a ratio of the initial modulation wavelength to that at the time of the measurement) was used as a measure of the drive to compare with predictions. The good agreement between measured and simulated wavelength evolution validated the drive modeling used in the simulations [10]. To determine the wavelengths, Fourier analysis on three central waves was used for each mode. Spherical effects introduced the error in determining the wavelength, which was greater for lower modes.

Figure 4 shows the evolution of the measured and simulated amplitudes of the optical-depth modulations for mode 30 with an initial amplitude of 0.75 μm [Fig. 4(a)], mode 60 with initial amplitudes of 1.7 and 0.25 μm [Fig. 4(b)], and mode 90 with an initial amplitude of 0.3 μm [Fig. 4(c)]. Simulations are shown by the solid and dashed curves for two plastic EOS models [30] used in ignition designs: LEOS 5400 and LEOS 5370, respectively. Simulated optical-depth modulations were obtained by postprocessing of simulations using a 5.4-keV backlighter and using measured spatial and temporal resolutions of the imaging system. The LEOS 5370 model corresponds to a slightly softer equation of state, compared to the LEOS

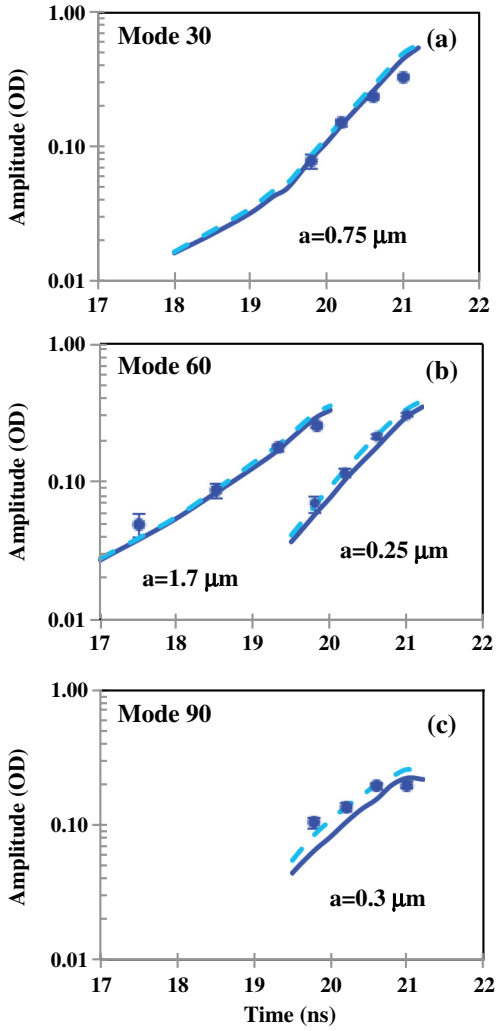

FIG. 4 (color online). Evolution of the measured and simulated amplitudes of the optical-depth modulations for (a) mode 30 and an amplitude of 0.75 μm, (b) mode 60 and amplitudes of 1.7 and 0.25 μm, and (c) mode 90 and an amplitude of 0.3 μm. Simulations are shown by the solid and dashed curves for two plastic EOS models: LEOS 5400 and LEOS 5370, respectively.

5400, leading to slightly larger predicted growth during the Richtmyer-Meshkov (shock transit) phase. At the relevant pressure range of 1–4 Mbar, the difference in compression is in the range from 4% to 7% between these two EOS models. Based on the simulations, about 80% of the shell has been ablated at the time of measurements. We note good agreement between data and simulations at all times and, in particular, over a range of 50× in modulation growth for mode 60 (combining low and high initial amplitude data). For mode 90 at 19.8 ns, the measured amplitude was slightly larger than predicted by using LEOS 5400 (by a factor of ~1.3) and LEOS 5370 (by a factor of 1.1), while the agreement was better at later times and for other modes. Compared to earlier hypotheses that growth factors might be 3–5 times larger than predicted for the

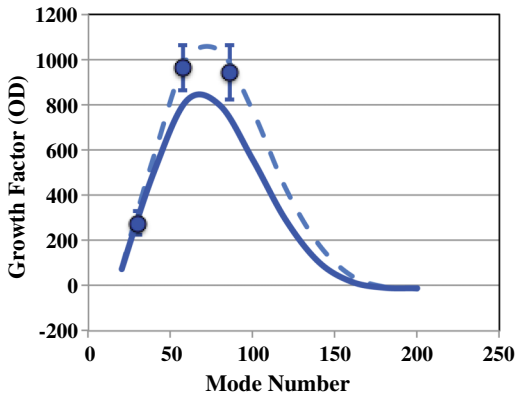

FIG. 5 (color online). Measured and calculated perturbation growth factors for optical-depth modulations as a function of the modulation mode number are shown at a shell radius of 650 μm, corresponding to a measurement time of 20.3 ns. Simulations are shown by the solid and dashed curves for two plastic EOS models: LEOS 5400 and LEOS 5370, respectively.

fastest growing modes [3], the experimental results were much closer to the predictions. The small discrepancies indicate that some of the physics used in the modeling (including the preheat due to Au M-band x rays of hohlraum emission, plastic equation of state, radiation transport, etc.) could still be improved.

Figure 5 shows measured and calculated modulation OD growth factors as a function of the modulation mode number at a shell radius of 650 μm, corresponding to a measurement time of 20.3 ns. The OD growth factor was defined as the ratio of the modulation OD amplitude at the time of the measurement to the initial modulation OD amplitude. Simulations are shown by the solid and dashed curves for two plastic EOS models: LEOS 5400 and LEOS 5370, respectively. Again, LEOS 5370, being softer, leads to slightly larger predicted growth, which appears to agree better with the experimental data. Peak growth factors of ~1000 are observed both experimentally and in the simulations at modes $\ell = 60$–80 and fall off sharply for modes 30 and less. The simulations predict that the growth factors drop rather sharply for modes $> \sim 100$ and do not appear to predict a significant negative lobe (growth factors <0). Effects of the spatial resolution were taken out in the measured experimental points for fair comparison. The good agreement between simulations and experiments indicated that instability growth was modeled well in cryogenic layered DT implosions for the most unstable modulations in the early stages of growth for the first 600 μm of the shell trajectory, up to convergence ratios of ~2. The results do not support the use of large surface-roughness multipliers, used to explain performance of the previous layered DT implosions [10]. This was the crucial result for a development of new ignition designs. Remaining to be tested is the acceleration-phase growth at higher mode numbers and to higher convergences, as well as the growth in the deceleration phase.

In conclusion, the first hydrodynamic instability growth measurements in indirectly driven implosions measured instability growth of preimposed modulations with Legendre mode numbers from 30 to 90 at the National Ignition Facility. The capsules were imploded by using ignition-relevant, low-adiabat ($\alpha \sim 1.5$) laser pulses, and ablation-front modulation growth was measured by using in-flight x-ray radiography for a shell convergence ratio of ~2. The measured growth was in good agreement with that predicted, thus validating simulations for the fastest growing modulations with mode numbers up to 90 early in the acceleration phase. It was a crucial first step in a focused set of experiments examining hydrodynamic-instability growth and mix. Future experiments will examine RT instability growth at higher convergence, for higher-mode number modulations, and during the deceleration phase.

This work was performed under the auspices of the U.S. Department of Energy by Lawrence Livermore National Laboratory under Contract No. DE-AC52-07NA27344.

[1] E. I. Moses, R. N. Boyd, B. A. Remington, C. J. Keane, and R. Al-Ayat, Phys. Plasmas **16**, 041006 (2009); G. H. Miller, E. I. Moses, and C. R. Wuest, Opt. Eng. (N.Y.) **43**, 2841 (2004).
[2] S. W. Haan *et al.*, Phys. Plasmas **18**, 051001 (2011).
[3] V. A. Smalyuk *et al.*, Phys. Rev. Lett. **111**, 215001 (2013).
[4] M. J. Edwards *et al.*, Phys. Plasmas **20**, 070501 (2013).
[5] S. P. Regan *et al.*, Phys. Plasmas **19**, 056307 (2012).
[6] S. P. Regan *et al.*, Phys. Rev. Lett. **111**, 045001 (2013).
[7] T. Ma *et al.*, Phys. Rev. Lett. **111**, 085004 (2013).
[8] S. Atzeni and J. Meyer-ter-Vehn, *The Physics of Inertial Fusion: Beam Plasma Interaction, Hydrodynamics, Hot Dense Matter*, International Series of Monographs on Physics (Clarendon, Oxford, 2004).
[9] J. D. Lindl, *Inertial Confinement Fusion: The Quest for Ignition and Energy Gain Using Indirect Drive* (Springer-Verlag, New York, 1998).
[10] D. S. Clark *et al.*, Phys. Plasmas **20**, 056318 (2013).
[11] Lord Rayleigh, *Scientific Papers II* (Cambridge University Press, Cambridge, England, 1900).
[12] G. I. Taylor, Proc. R. Soc. A **201**, 192 (1950).
[13] H. Azechi, T. Sakaiya, S. Fujioka, Y. Tamari, K. Otani, K. Shigemori, M. Nakai, H. Shiraga, N. Miyanaga, and K. Mima, Phys. Rev. Lett. **98**, 045002 (2007).
[14] R. D. Richtmyer, Commun. Pure Appl. Math. **13**, 297 (1960).
[15] E. E. Meshkov, Izv. Acad. Sci. USSR, Fluid Dynamics **4**, 101 (1969).
[16] R. H. H. Scott *et al.*, Phys. Rev. Lett. **110**, 075001 (2013).
[17] O. L. Landen *et al.*, Plasma Phys. Controlled Fusion **54**, 124026 (2012).
[18] S. W. Haan *et al.*, Fusion Sci. Technol. **63**, 67 (2013).
[19] V. A. Smalyuk, S. Hu, J. Hager, J. Delettrez, D. Meyerhofer, T. Sangster, and D. Shvarts, Phys. Rev. Lett. **103**, 105001 (2009).
[20] A. Casner *et al.*, Phys. Plasmas **16**, 092701 (2009).
[21] D. G. Hicks *et al.*, Phys. Plasmas **19**, 122702 (2012).
[22] D. A. Callahan *et al.*, Phys. Plasmas **19**, 056305 (2012).
[23] N. B. Meezan *et al.*, Phys. Plasmas **20**, 056311 (2013).
[24] H. F. Robey *et al.*, Phys. Rev. Lett. **108**, 215004 (2012).
[25] H. F. Robey *et al.*, Phys. Plasmas **19**, 042706 (2012).
[26] S. H. Glenzer *et al.*, Phys. Plasmas **19**, 056318 (2012).
[27] S. Glenn *et al.*, Rev. Sci. Instrum. **81**, 10E539 (2010).
[28] W. L. Kruer, *The Physics of Laser Plasma Interactions* (Addison-Wesley, Reading, MA, 1988).
[29] T. Döppner *et al.*, Phys. Rev. Lett. **108**, 135006 (2012).
[30] S. Hamel *et al.*, Phys. Rev. B **86**, 094113 (2012).